Handbook of Neuroimaging Data Analysis

8

Image Reconstruction in Functional MRI

Daniel B. Rowe
Department of Mathematics, Statistics, and Computer Science
Marquette University

CONTENTS

8.1 Introduction

In the world we live in with all of our technological advances, we still have a relatively poor understanding of how the healthy human brain works, let alone how it is disfunctioning due to disease or injury. Our brain is one of the most complicated systems in the universe, which is exactly what makes it one of the last but most exciting scientific frontiers. Magnetic resonance imaging (MRI), for which Drs. Paul Lauterbur and Peter Mansfield won the 2003 Nobel Prize, is an ideal noninvasive imaging technique to see inside the human brain.

Structural or anatomical MRI has been an invaluable tool for the diagnosis and monitoring of human neurological ailments. Functional MRI (fMRI) is a lesser known type of MRI that allows us to observe the cognitively active brain in action. In 1992 there were three fMRI publications in close succession: the first by Bandettini (1), the second by Kwong (2) and the third by Ogawa (3). These three papers established fMRI with the blood-oxygen-level-dependent (BOLD) signal, which is a neural correlate and does not require exogenous contrast.

In MRI and fMRI, the measurements taken by the scanner are not voxel values. The actual measurements taken by the scanner are to a good approximation, complex-valued (real and imaginary) spatial frequencies. Small magnetic field gradients are, changed in time that result in changing location in spatial frequency space. While changing spatial frequency location, complex-valued spatial frequency measurements are taken. This Chapter aims to provide the reader with the necessary technical abilities and conceptual understandings to perform and understand fMRI image reconstruction and processing. The outline of the chapter is as follows. Section 8.2 describes the discrete Fourier transform, which is absolutely invaluable for understanding fMRI measurements. Section 8.3 describes Fourier encoding and complex-valued fMRI measurements that are discrete inverse Fourier transform reconstructed into a complex-valued image. Section 8.4 presents the discrete inverse Fourier image reconstruction process with an isomorphism representation so that signal and image processing steps can be described and their effects quantified. Section 8.5 summarizes the additional related topic of complex-valued time series activation models and a discussion reviewing the covered topics and future areas. In this chapter, the magnetic resonance (MR) physics will not be described, but the basic measurement and image reconstruction processes will be discussed. The discussion here will be limited to Cartesian k-space spatial frequency sampling.

8.2 The Fourier Transform

As previously noted, the measurements taken by the MRI scanner are, to a good approximation, complex-valued spatial frequencies. That is, the measurements taken by the scanner are ideally the Fourier transform (4) of the object being imaged. In this section, the one-dimensional discrete Fourier transform and discrete inverse Fourier transform will be described then extended to the two-dimensional discrete Fourier transform and inverse Fourier transform. What we will see is that regardless of whether we have a one-dimensional or two-dimensional signal, the Fourier transform selects out the constituent cosine and sine frequencies that make up the signal. In Section 8.3 we will see that the MRI scanner measures (to a good approximation) the constituent cosine and sine frequencies in an image and we inverse Fourier transform these frequencies in order to reconstruct an image.

8.2.1 One-Dimensional Fourier Transform

The mathematics for the one-dimensional discrete Fourier transform will be described then an example involving a time series of measurements will be presented. The one-dimensional discrete Fourier transform $F(q\Delta\nu)$ of a time series $y(t)$ sampled at N times Δt apart is defined as in Equation 8.1 below

$$f(q\Delta\nu) \quad = \quad \sum_{p=1}^{N} y(p\Delta t) e^{-i2\pi(p-1)(q-1)/N} \tag{8.1}$$

for $p, q = 1, \ldots, N$. The difference in temporal frequency $\Delta\nu$ between $f(q\Delta\nu)$ and $f((q+1)\Delta\nu)$ is $\Delta\nu = 1/(N\Delta t)$ with $i = \sqrt{-1}$ being the imaginary unit. The one-dimensional discrete Fourier transform $f(q\Delta\nu)$ at a given frequency $q\Delta\nu$ in general consists of both a real and an imaginary part. In order to satisfy the very important Shannon–Nyquist sampling criteria (5, 6), which allows the resolution of temporal frequencies, the time series must be sampled at twice its highest constituent temporal frequency. The highest temporal

frequency that can be resolved and hence the bounds on the horizontal frequency axis is $\nu_{max} = 1/(2\Delta t)$. If the time series being discrete Fourier transformed is completely real-valued, then the discrete temporal frequencies have Hermitian symmetry where the bottom half is the conjugate transpose of the top half.

With the zero frequency of the frequency spectrum centered, the one-dimensional discrete inverse Fourier transform of $f(q\Delta\nu)$ is defined as in Equation 8.2 below

$$y(p\Delta t) \quad = \quad \frac{1}{N} \sum_{q=-N/2}^{N/2-1} f(q\Delta\nu) e^{+i2\pi pq/N} \tag{8.2}$$

for $p, q = -N/2, \ldots, N/2 - 1$. The time series will be ordered from the first time point to the last. This definition of the one-dimensional discrete inverse Fourier transform will be utilized because MRI and fMRI measurements have the zero frequency centered and there is generally an even number of measurements. The discrete inverse Fourier transform $y(p\Delta t)$ at a given time point p in general consists of both a real and an imaginary part, but this imaginary part may be zero.

The one-dimensional forward discrete Fourier transformation procedure described in Equation 8.1 can be equivalently written as

$$(f_R + if_I) \quad = \quad \left(\bar{\Omega}_R + i\bar{\Omega}_I\right) \quad (y_R + iy_I) \tag{8.3}$$

where $y_R = (y_R(1\Delta t), \ldots, y_R(N\Delta t))'$ and $y_I = (y_I(1\Delta t), \ldots, y_I(N\Delta t))'$, are the real and imaginary parts of the measured time series while $f_R = (f_R(1\Delta\nu), \ldots, f_R(N\Delta\nu))'$ and $f_I = (f_I(1\Delta\nu), \ldots, f_I(N\Delta\nu))'$ are the real and imaginary parts of the one-dimensional discrete Fourier transform of the time series (temporal frequencies). The Fourier matrix $\bar{\Omega} = (\bar{\Omega}_R + i\bar{\Omega}_I)$ in Equation 8.3 is given by

$$\bar{\Omega} = \begin{pmatrix} 1 & 1 & \cdots & 1 \\ 1 & W & & W^N \\ \vdots & \vdots & \ddots & \vdots \\ & & & W^{(N-1)N} \\ 1 & W^N & & W^{N*N} \end{pmatrix} \tag{8.4}$$

where $W = e^{-\frac{i2\pi}{N}}$ is an *a priori* known quantity from the sampling plan. The jkth element (row j and column k) of $\bar{\Omega}_R$ and $\bar{\Omega}_I$ are $\cos(2\pi(j-1)(k-1)/N)$ and $\sin(2\pi(j-1)(k-1)/N)$ where $j, k = 1, \ldots, N$.

Similarly, the one-dimensional discrete inverse Fourier transformation procedure described in Equation 8.2 can be equivalently written as

$$(y_R + iy_I) \quad = \quad (\Omega_R + i\Omega_I) \quad (f_R + if_I) \tag{8.5}$$

where variables are as previously defined. The inverse Fourier matrix $\Omega = (\Omega_R + i\Omega_I)$ in Equation 8.5 is given by

$$\Omega = \begin{pmatrix} W^{(-\frac{N}{2})(-\frac{N}{2})} & W^{(-\frac{N}{2})(-\frac{N}{2}+1)} & \cdots & W^{(-\frac{N}{2})(\frac{N}{2}-1)} \\ W^{(-\frac{N}{2}+1)(-\frac{N}{2})} & W^{(-\frac{N}{2}+1)(-\frac{N}{2}+1)} & & W^{(-\frac{N}{2}+1)(\frac{N}{2}-1)} \\ & & \ddots & \vdots \\ & & & W^{(\frac{N}{2}-2)(\frac{N}{2}-1)} \\ W^{(\frac{N}{2}-1)(-\frac{N}{2})} & & & W^{(\frac{N}{2}-1)(\frac{N}{2}-1)} \end{pmatrix} \tag{8.6}$$

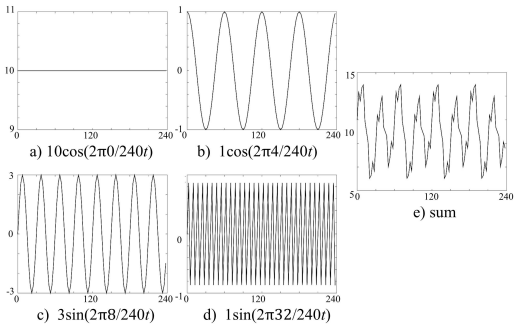

FIGURE 8.1
Discrete constituent parts and their sum for the one-dimensional function.

where $W = e^{\frac{i2\pi}{N}}$. The jkth element of Ω_R and Ω_I are $\cos(2\pi(j - N/2 - 1)(k - N/2 - 1)/N)$ and $\sin(2\pi(j - N/2 - 1)(k - N/2 - 1)/N)$.

The one-dimensional discrete Fourier transform can be illustrated with an example. A continuous one-dimensional signal $y(t)$ as in Equation 8.7 below

$$y(t) = 10\cos\left(2\pi\frac{0}{240}t\right) + \cos\left(2\pi\frac{4}{240}t\right) + 3\sin\left(2\pi\frac{8}{240}t\right) + \sin\left(2\pi\frac{32}{240}t\right) \tag{8.7}$$

is sampled at time $t = (p-1)\Delta t$ for $p = 1, \ldots, N$, $N = 96$, and $\Delta t = 2.5$ s (seconds) for a total of 240 s. The four discrete functions composing $y(p\Delta t)$ are presented in Figures 8.1a–d with their sum $y(p\Delta t)$ being in Figure 8.1e. The units for the horizontal axis in Figure 8.1 is seconds.

The one-dimensional discrete Fourier transform of $y(p\Delta t)$ for $p = 1, \ldots, N$ is given in Figure 8.2. After the one-dimensional discrete Fourier transform, the frequency spectrum was shifted so that the zero frequency is centered. What can be seen in Figure 8.2 is that the one-dimensional discrete Fourier transformation process selects out the constituent temporal frequencies. The units for the horizontal axes in Figure 8.2 is 1/s (cycles per second or Hz). In Figure 8.2 there are points (that have been connected) at the temporal frequencies that make up the time series. The real part of the temporal frequency spectrum in Figure 8.2a contains the cosine frequencies and the imaginary part in Figure 8.2b contains the sine frequencies. The magnitude in Figure 8.2c is a typical way of representing all the constituent frequencies with phase between the frequency parts in Figure 8.2d. There is a peak in the middle of Figure 8.2a (where the full vertical scale is limited to 96), corresponding to the zero cosine frequency (constant or baseline term) and at $4/240 \approx 0.0167$ Hz. We can also see points in Figure 8.2b are the $8/240 \approx 0.0333$ Hz and $32/240 \approx 0.1333$ Hz sine frequencies. The heights of the points are $NA_\nu/2$, where A_ν is the amplitude of the sinusoid at frequency ν except for the zero frequency, which has a height of NA_0. Also note that the real part is symmetric while the imaginary part is anti-symmetric.

A pictorial depiction of the one-dimensional discrete Fourier transform can be seen by displaying the time series as an image as in Figure 8.3. Again, after the discrete Fourier transform, the frequency spectrum was shifted so that the zero frequency is centered. In Figure 8.3c are the real (left) and imaginary (right) parts of the time series (intensity limited from 5 to 15), in Figure 8.3b are the real (left) and imaginary (right) parts of the Fourier matrix (intensity limited from -1 to 1), and in Figure 8.3a are the real (left) and imaginary (right) parts of the frequency spectrum (intensity limited from 0 to 96). The units for the vertical axis in Figure 8.3a is Hertz and for Figure 8.3c seconds. In this chapter, the greyscale for all images will use the convention that black will depict lower values and white,

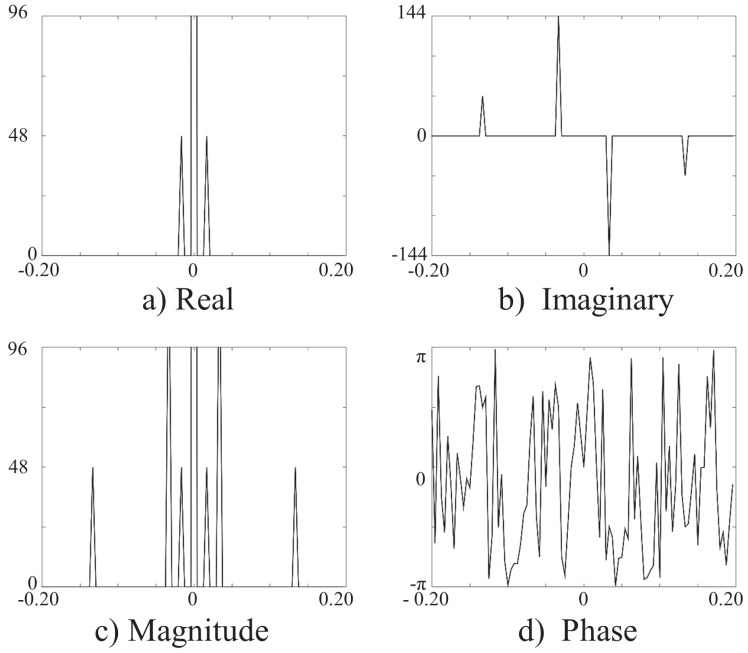

FIGURE 8.2
Fourier transform of the time series.

higher values. Note that the intensity values of the horizontal stripes in Figure 8.3c (left) are brighter for higher values and depict the time series in Figure 8.1e.

Again, we can see that the one-dimensional discrete Fourier transform selects out the constituent temporal frequencies of the time series. The cosine frequencies are represented in Figure 8.3a (left) and the sines in Figure 8.3a (right).

In the same fashion, the inverse Fourier transform can be depicted as in Figure 8.4. The units for the axes in Figure 8.4a is seconds and Figure 8.4c Hertz. In Figure 8.4c are the real (left) and imaginary (right) parts to the frequency spectrum, in Figure 8.4b are the real

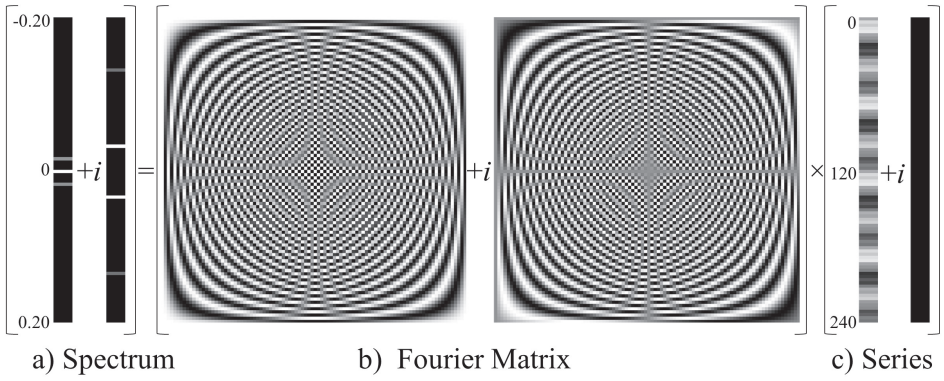

FIGURE 8.3
Matrix representation of one-dimensional discrete Fourier transform.

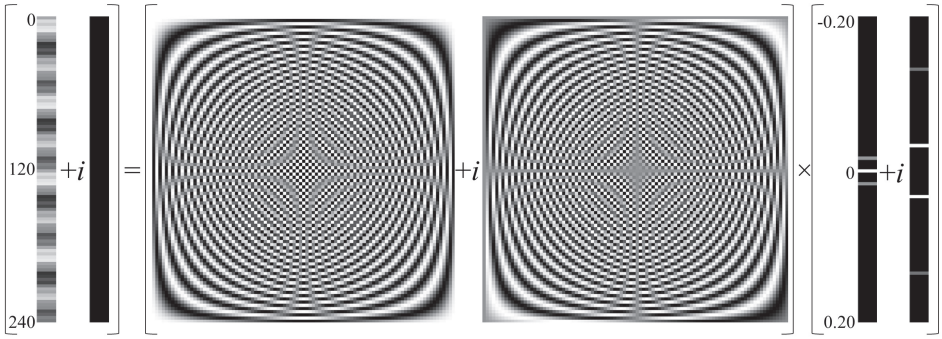

FIGURE 8.4
Matrix representation of one-dimensional discrete inverse Fourier transform.

(left) and imaginary (right) parts of the one-dimensional discrete inverse Fourier transform matrix (intensity limited from $-1/96$ to $1/96$), and in Figure 8.4a are the real (left) and imaginary (right) parts of the time series as originally specified.

We can see that when we have measured the constituent complex-valued frequencies, we can inverse Fourier transform reconstruct them into the measured time series. Although the one-dimensional discrete Fourier transform and discrete inverse Fourier transforms in Equation 8.3 and Equation 8.5 have a great conceptual interpretation, the implementations in Equation 8.1 and Equation 8.2 are computationally faster and generally how the transforms are performed. In Section 8.4, the discrete Fourier transform and discrete inverse Fourier transforms will be represented with an isomorphism that has an even better conceptual interpretation that is useful for statistical purposes. In MRI and fMRI, the measurements taken by the scanner are, to a good approximation, discrete complex-valued spatial frequencies and we reconstruct them into a discrete complex-valued image via the discrete inverse Fourier transform. The discrete Fourier transform and discrete inverse Fourier transform are reverse operations, meaning that you can one-dimensional discrete forward Fourier transform a time series to get temporal frequencies and then one-dimensional discrete inverse Fourier transform the temporal frequencies to get back the original time series. The discrete complex-valued frequencies can be obtained from the discrete complex-valued time series and vice versa provided there is no loss of data.

8.2.2 Two-Dimensional Fourier Transform

The mathematics for the two-dimensional discrete Fourier transform will be described similar to the way that it was done for the one-dimensional discrete Fourier transform, then an example involving an illustrative sample image will be presented. The two-dimensional discrete Fourier transform $F(q_x\Delta k_x, q_x\Delta k_x)$ of an image Y sampled at N_x horizontal and N_y vertical locations Δx and Δy distances apart is defined as in Equation 8.8 below

$$F(q_x\Delta k_x, q_y\Delta k_y) = \sum_{p_y=1}^{N_y}\sum_{p_x=1}^{N_x} Y(p_x\Delta x, p_y\Delta y)e^{-i2\pi(\frac{(p_x-1)(q_x-1)}{N_x}+\frac{(p_y-1)(q_y-1)}{N_y})} \tag{8.8}$$

for $p_x, q_x = 1, \ldots, N_x$ and $p_y, q_y = 1, \ldots, N_y$. The differences in spatial frequencies between successive values Δk_x and Δk_y are $\Delta k_x = 1/(N_x\Delta x)$ and $\Delta k_y = 1/(N_y\Delta y)$. In order to satisfy the very important Shannon–Nyquist sampling criteria that allows the resolution

of spatial frequencies, the image must be sampled at twice the highest constituent spatial frequency in each dimension. The highest spatial frequencies that can be resolved and hence the bounds on the two frequency axes are $k_{x,max} = 1/(2\Delta x)$ and $k_{y,max} = 1/(2\Delta y)$. If the image being discrete Fourier transformed is completely real-valued, then the discrete spatial frequencies have Hermitian symmetry where the bottom half is the conjugate transpose of the top half. Hermitian symmetry is generally not achieved in experimentally measured fMRI spatial frequencies. The two-dimensional discrete Fourier transform $F(q_x\Delta k_x, q_y\Delta k_y)$ at a given frequency pair $(q_x\Delta k_x, q_y\Delta k_y)$ in general consists of both a real and an imaginary part.

With the zero frequency of the frequency spectrum centered, the two-dimensional discrete inverse Fourier transform of $F(q_x\Delta k_x, q_y\Delta k_y)$ is defined as in Equation 8.9 below

$$Y(p_x\Delta x, p_y\Delta y) = \frac{1}{N_x N_y} \sum_{q_y=-N_y/2}^{N_y/2-1} \sum_{q_x=-N_x/2}^{N_y/2-1} F(q_x\Delta k_x, q_y\Delta k_y) e^{+i2\pi(\frac{p_x q_x}{N_x} + \frac{p_y q_y}{N_y})} \tag{8.9}$$

for $p_x, q_x = -N_x/2, \ldots, N_x/2 - 1$ and $p_y, q_y = -N_y/2, \ldots, N_y/2 - 1$. It should be noted that it is not necessarily the case that $N_x = N_y$ or that $\Delta x = \Delta y$. The image will be ordered from the first pixel or voxel to the last in both dimensions. This definition of the two-dimensional discrete inverse Fourier transform will be utilized because MRI and fMRI measurements have the zero frequency centered and generally an even array size in each dimension is measured. The two-dimensional discrete inverse Fourier transform of the image $Y(p_x\Delta x, p_y\Delta y)$, at a given voxel $(p_x\Delta x, p_y\Delta y)$ in general consists of both a real and an imaginary part, but this imaginary part may be zero.

The two-dimensional forward discrete Fourier transformation procedure described in Equation 8.8 can be equivalently written as

$$(F_R + iF_I) \quad = \quad \left(\bar{\Omega}_{yR} + i\bar{\Omega}_{yI}\right) \quad (Y_R + iY_I) \quad \left(\bar{\Omega}_{xR} + i\bar{\Omega}_{xI}\right)^T \tag{8.10}$$

where T denotes the transpose, Y_R and Y_I are the real and imaginary parts of the measured image, and F_R and F_I are the real and imaginary parts of the Fourier transform of the image (spatial frequencies). If we have a real-valued image, then the imaginary part of the image Y_I is zero. The two-dimensional discrete Fourier matrices $\bar{\Omega}_x$ and $\bar{\Omega}_y$ in Equation 8.10 are the same as in the one-dimensional discrete Fourier transform in Equation 8.4 with appropriate dimensions.

The two-dimensional discrete inverse Fourier transformation procedure described in Equation 8.9 can be equivalently written as

$$(Y_R + iY_I) \quad = \quad \left(\Omega_{yR} + i\Omega_{yI}\right) \quad (F_R + iF_I) \quad \left(\Omega_{xR} + i\Omega_{xI}\right)^T \tag{8.11}$$

where variables are all as previously defined. The discrete inverse Fourier matrices Ω_x and Ω_y in Equation 8.11 are the same as in the one-dimensional discrete inverse Fourier transform in Equation 8.6 with appropriate dimensions.

Similar to the one-dimensional discrete Fourier transform, the two-dimensional discrete Fourier transform can be illustrated with an example. A continuous two-dimensional image $Y(x, y)$ as in Equation 8.12 below

$$\begin{aligned} Y(x,y) \quad = \quad & 10\cos\left(2\pi\frac{0}{240}x\right) + \frac{3}{2}\cos\left(2\pi\frac{8}{240}x\right) \\ & + \sin\left(2\pi\frac{24}{240}y\right) + \cos\left(2\pi\frac{16}{240}x + 2\pi\frac{16}{240}y\right) \end{aligned} \tag{8.12}$$

is sampled at position $x = (p_x - 1)\Delta x$ and $y = (p_y - 1)\Delta y$ for $p_x = 1, \ldots, N_x$, $p_y = 1, \ldots, N_y$,

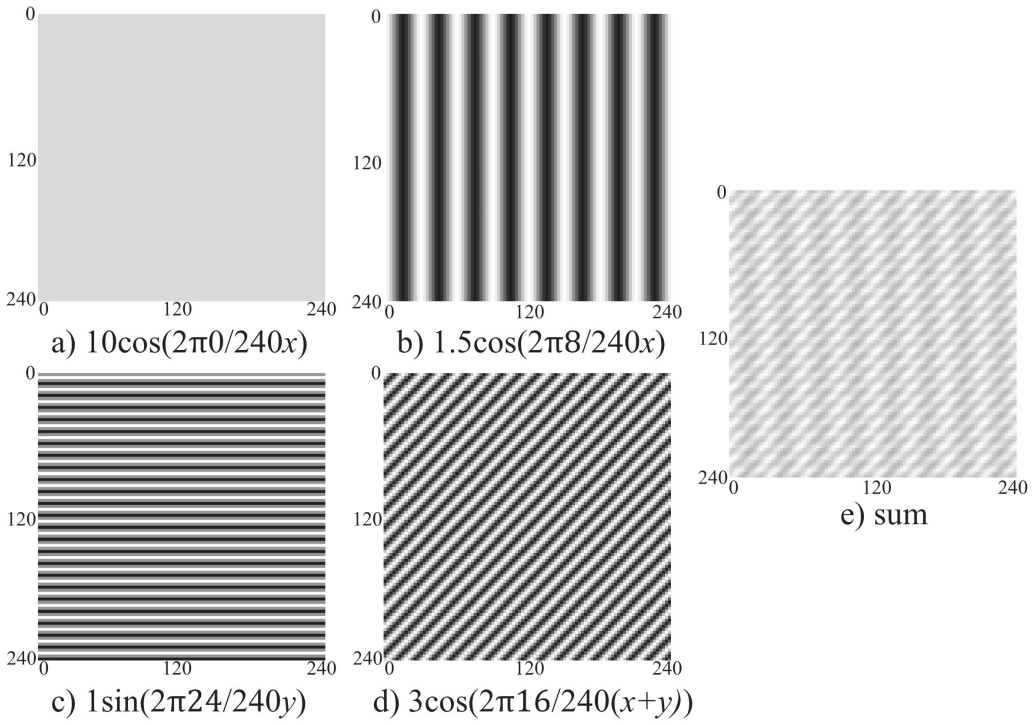

FIGURE 8.5
Discrete constituent parts and their sum for the two-dimensional image.

$N_x = 96$, $N_y = 96$, and $\Delta x = \Delta y = 2.5$ mm (millimeters) corresponding to a 240-mm field of view. The four discrete functions composing $Y(p_x\Delta x, p_y\Delta y)$ are presented in Figures 8.5a–d with their sum $Y(p_x\Delta x, p_y\Delta y)$ being in Figure 8.5e. The units for the axes in Figure 8.5 are millimeters.

What can be seen in Figure 8.6 is that the two-dimensional discrete Fourier transformation process again selects out the constituent spatial frequencies. After the two-dimensional discrete Fourier transform, the frequency spectrum was shifted so that the zero frequency is centered. In Figure 8.6c are the real (top) and imaginary (bottom) parts of the image (intensity limited from -15 to 15), in Figures 8.6b and d are the real (top) and imaginary (bottom) parts of the Fourier matrices (intensity limited from -1 to 1), and in Figure 8.6a are the real (top) and imaginary (bottom) parts of the frequency spectrum (intensity limited from 0 to 96^2). The units for the image in Figure 8.6c are millimeters and spatial frequencies in 8.6a are mm^{-1} (wave number). The transpose of $\bar{\Omega}_x$ is displayed in Figure 8.6d.

There are points at the spatial frequencies that make up the image. The real part of the spatial frequency spectrum contains the cosine frequencies and the imaginary part contains the sine frequencies. There is a peak in the middle of Figure 8.6a (top) corresponding to the zero cosine frequency (constant or baseline term), at the $8/240 \approx 0.0333$ mm^{-1} x spatial frequency, and at the $24/240 = 0.1000$ mm^{-1} both x and y spatial frequency. Also, we can see points in Figure 8.6a (bottom) at the $16/240 \approx 0.0667$ mm^{-1} spatial frequency. The heights of the points are $N_x N_y A_{k_x,k_y}/4$, where A_{k_x,k_y} is the amplitude of the planar sinusoid at frequency (k_x, k_y) except for the zero frequency, which has a height of $N_x N_y A_{0,0}$. It is important to note that the real part is symmetric while the imaginary

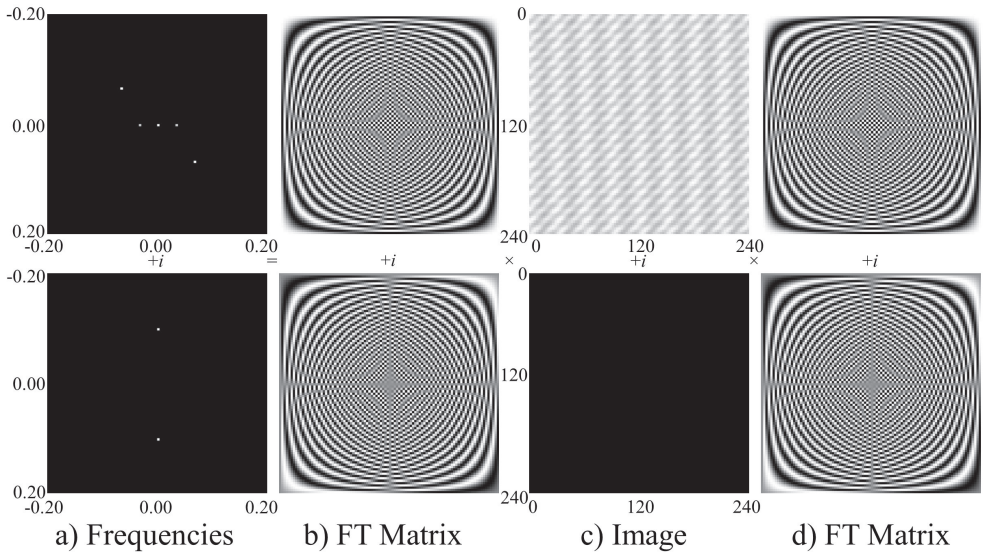

FIGURE 8.6
Matrix representation of two-dimensional discrete Fourier transform.

part is anti-symmetric, but for display purposes the intensities of the imaginary part were made completely positive.

In the same fashion, the inverse Fourier transform can be depicted as in Figure 8.7. In Figure 8.7c are the real (top) and imaginary (bottom) parts of the frequency spectrum, in Figure 8.7b and Figure 8.7d are the real (top) and imaginary (bottom) parts of the two-dimensional discrete inverse Fourier transform matrices (intensity limited from $-1/96$ to $1/96$ for Figure 8.7b and from $-1/96$ to $1/96$ for Figure 8.7d). Note the difference in appearance between Figure 8.6b and Figure 8.7b. In Figure 8.7a are the real (top) and imaginary (bottom) parts of the two-dimensional discrete inverse Fourier transformed image. The image being presented in Figure 8.7d is the transpose of Ω_x.

We can see that when we have measured the constituent complex-valued frequencies of an image, we can reconstruct them into the measured image. Although the discrete Fourier transform and discrete inverse Fourier transforms in Equation 8.10 and Equation 8.11 have a great conceptual interpretation, the implementations in Equation 8.8 and Equation 8.9 are computationally faster and most often how performed. In Section 8.4, the discrete Fourier transform and discrete inverse Fourier transforms will be represented with an isomorphism that has an even better conceptual interpretation and is useful for statistical analysis. In MRI and fMRI, the measurements taken by the scanner are, to a good approximation, complex-valued spatial frequencies and we reconstruct them into a complex-valued image via the discrete inverse Fourier transform.

The discrete Fourier transform and discrete inverse Fourier transform are reverse operations, meaning that you can two-dimensional discrete forward Fourier transform an image to get spatial frequencies then two-dimensional discrete inverse Fourier transform the spatial frequencies to get back the original image. The discrete complex-valued frequencies can be obtained from the discrete complex-valued time series and vice versa provided there is no loss of data. The discrete Fourier transform and discrete inverse Fourier transform are reverse operations provided there is no loss of data such as discarding phase images as is common in fMRI.

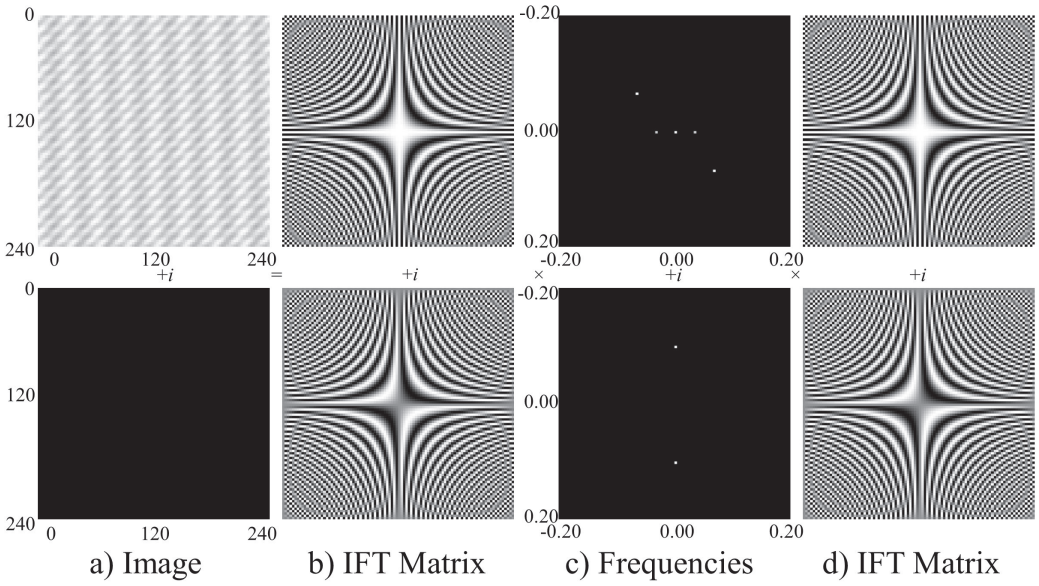

FIGURE 8.7
Matrix representation of two-dimensional discrete inverse Fourier transform.

8.3 FMRI Acquisition and Reconstruction

It was important to review the one and two dimensional discrete Fourier transforms along with their inverses in Section 8.2 to prepare for measured fMRI data. In Section 8.2, it was seen that the two-dimensional discrete complex-valued spatial frequencies could be two dimensional discrete inverse Fourier transform reconstructed into a complex-valued image. In MRI and fMRI, the data measured by the scanner is, to a good approximation, the Fourier transform of the object being imaged (4). The spatial frequencies, called k-space, are measured by the scanner and inverse Fourier transform reconstructed into a complex-valued image. In this section, the MR signal equation is described along with a standard fMRI gradient echo–echo planar imaging (GRE-EPI) pulse sequence and the coverage of k-space (spatial frequencies).

8.3.1 The Signal Equation and k-Space Coverage

Without delving into the MRI physics, the continuous signal $s(k_x, k_y)$ to be measured by the scanner at time $t(k_x, k_y)$ for k-space location (k_x, k_y) is given by the following fairly general expression called the signal equation

$$\begin{aligned} s(k_x, k_y) &= \int_{-\infty}^{\infty}\int_{-\infty}^{\infty} \rho(x,y) e^{-i2\pi(k_x x + k_y y)} dx dy \\ k_x(t(k_x, k_y)) &= \frac{\gamma}{2\pi}\int_0^{t(k_x,k_y)} G_x(\tau) d\tau \\ k_y(t(k_x, k_y)) &= \frac{\gamma}{2\pi}\int_0^{t(k_x,k_y)} G_y(\tau) d\tau \end{aligned} \tag{8.13}$$

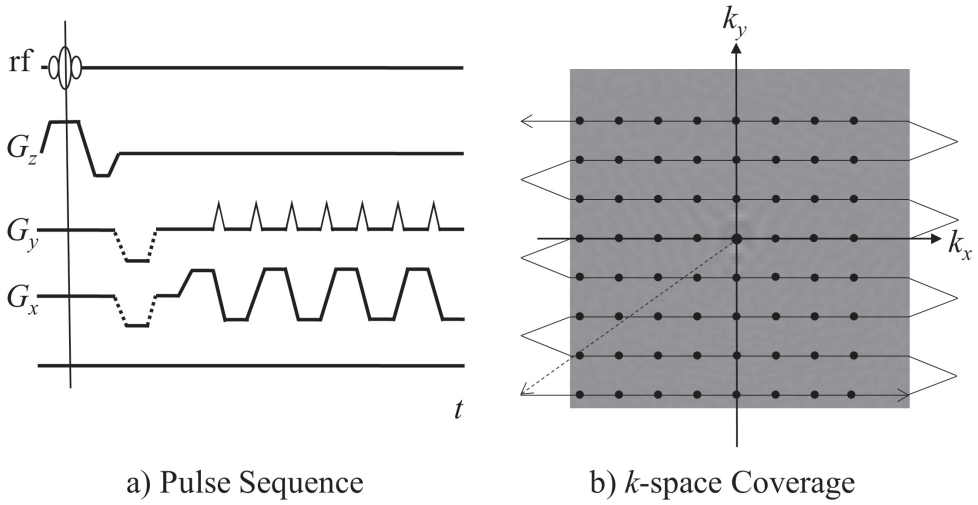

FIGURE 8.8
Standard GRE-EPI pulse sequence and k-space coverage.

where

$$\rho(x,y) = \rho_0(x,y)\left(1 - e^{TR/T_1(x,y)}\right) e^{t(k_x,k_y)/T_2^*(x,y)} e^{i\gamma\Delta B(x,y)t(k_x,k_y)} \ . \tag{8.14}$$

In Equation 8.14, $s(k_x, k_y)$ is the measured k-space signal at location (k_x, k_y), $\rho_0(x, y)$ is the proton spin density at position (x, y), $T_1(x, y)$ is the longitudinal relaxation at position (x, y), $T_2^*(x, y)$ is the transverse relaxation at position (x, y), $\Delta B(x, y)$ is the magnetic field inhomogeneity at position (x, y), TR is the time to repetition for measurement of the same slice, $\gamma = 2.67513 \times 10^8$ rad $\mathrm{s}^{-1}T^{-1}$ is the gyromagnetic ratio of the H^1 nucleus, and $G_x(\tau)$ and $G_y(\tau)$ are magnetic field gradients. We can see that $\rho(x, y)$ is not strictly a function of position but varies depending on the time that a k-space point is to be measured, so the Fourier relationship is an approximate one.

This is the two-dimensional continuous Fourier encoding expression upon which the previous discrete two-dimensional discrete inverse Fourier transform image reconstruction in Section 8.2 was based. By changing the magnetic field gradients $G_x(t)$ and $G_y(t)$ through time t, the signal that is to be measured corresponds to the different locations in k-space.

The way that k-space is traversed and complex-valued data measured is with the use of magnetic field gradients that are in addition to but much smaller than the main magnetic field. The changing of the G_x and G_y magnetic field gradients can be graphically described using what is called a pulse sequence diagram. In a pulse sequence diagram, multiple gradient waveforms are presented where the gradient strength (either positive or negative) is on the vertical axis and time is on the horizontal axis.

A standard GRE-EPI pulse sequence diagram is presented in Figure 8.8a and corresponding k-space coverage trajectory in Figure 8.8b. In Figure 8.8a, a radio frequency pulse at the beginning of the first waveform trace is applied to tip the magnetization into the transverse plane (called excitation) and a gradient G_z selects the slice to be imaged in the second waveform trace. At this time, we are at the center of k-space, $(k_x, k_y) = (0, 0)$. After excitation and slice selection, gradient magnetic fields are applied as seen in the first negative

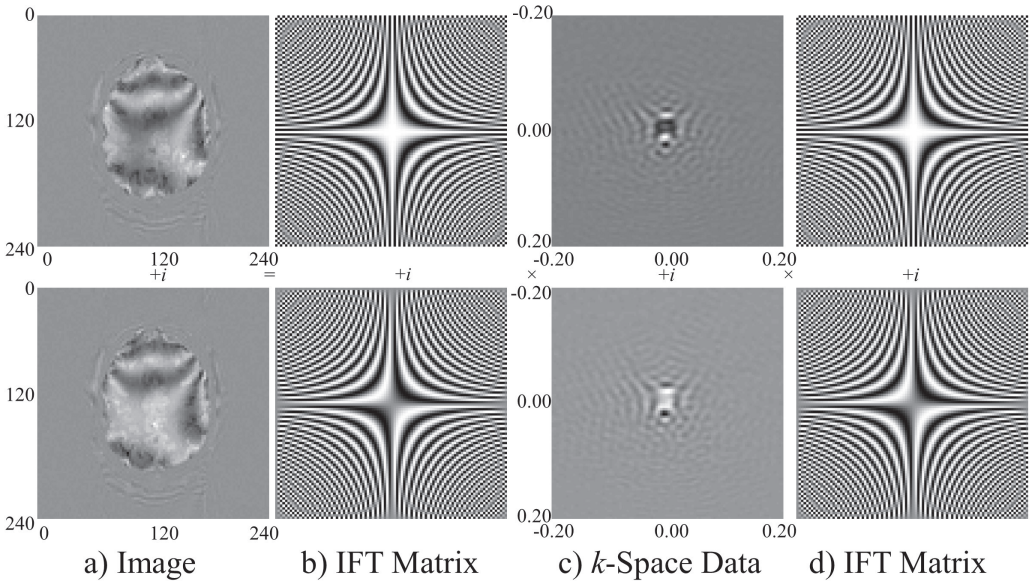

FIGURE 8.9
Matrix representation of fMRI image reconstruction.

trapezoidal-shaped changes in the G_y and G_x gradient waveforms (third and fourth traces). The initial negative trapezoidal G_y gradient takes us to the bottommost (most negative) k_y location while the initial negative trapezoidal G_x gradient takes us to the leftmost (most negative) k_x location. At this time, we are now at the bottom left corner of our k-space region. We apply a positive G_x gradient that takes us from left to right along the bottommost line of k-space. When we have reached the rightmost portion of k-space, we now apply a negative G_x gradient to take us from right to left in k-space and a positive triangular G_y gradient that takes up a k-space line. This process repeats until all of k-space is covered and complex-valued k-space array measurements are taken to fill in an array. The direction that we travel along lines of k-space is called the frequency encoding direction (k_x in this case) and the direction that we step up to travel along lines is called the phase encoding direction (k_y in this case). The trajectory that just described the coverage of k-space is illustrated in Figure 8.8b from bottom left to top left (with underlay being a lighter version of the real k-space array in Figure 8.9c).

The complex-valued k-space data (spatial frequencies) corresponding to an experimentally measured slice from a human fMRI scan (7) are displayed in Figure 8.9c. Note that the real part (cosines) and imaginary part (sines) of the k-space array is completely filled, unlike the simple illustrative example in Figure 8.7 of Section 8.2. The discrete inverse Fourier transform process is applied to the measured k-space data in Figure 8.9. The measured k-space data is in Figure 8.9c, the discrete inverse Fourier transform matrices are in Figure 8.9b and Figure 8.9d with the reconstructed (two-dimensional discrete inverse Fourier transformed) complex-valued image in Figure 8.9a. The two-dimensional discrete inverse Fourier transformation process as performed in Figure 8.7 of Section 8.2 reconstructs the experimentally measured k-space data into a complex-valued image. Note that the two discrete inverse Fourier transform matrices in Figure 8.7 are identical to those in Figure 8.9.

The reconstructed image in Figure 8.9a is in terms of real and imaginary parts. In most fMRI studies, the reconstructed images are transformed from Cartesian coordinates

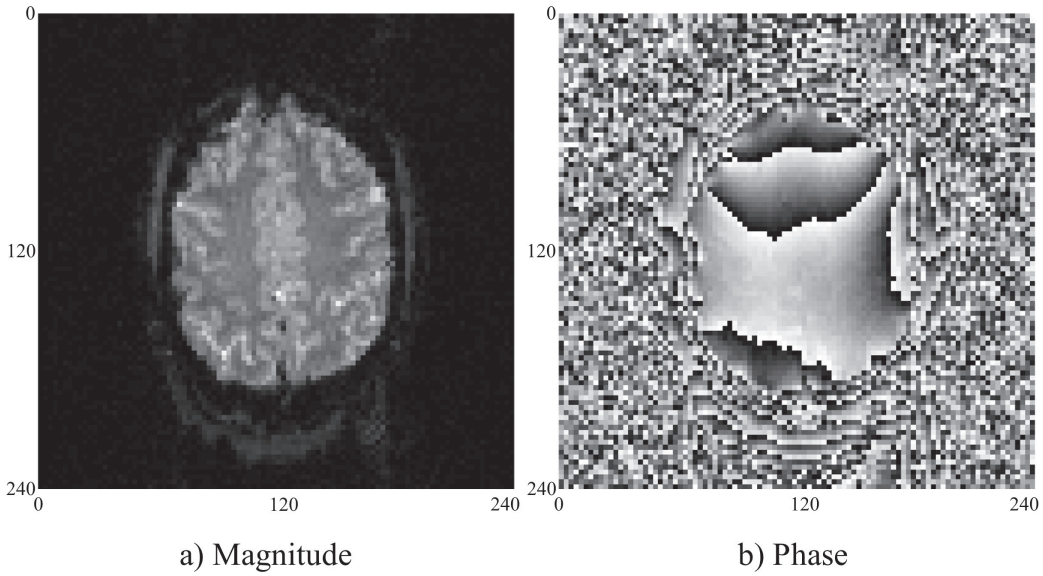

FIGURE 8.10
Magnitude and phase of real and imaginary reconstructed image.

of real and imaginary to polar coordinates of magnitude and phase as seen in Figure 8.10. This transformation changes the statistical properties of the images. Further, in most fMRI studies, the phase half of the reconstructed image data as in Figure 8.10b is discarded and only the magnitude images as in Figure 8.10a are included in statistical analysis, in addition to processing performed on the images as will be briefly described in Section 8.4. From a statistical perspective, we should utilize all of our measured data as will be summarized in Section 8.5.

8.3.2 Nyquist Ghost k-Space Correction

When experimental fMRI k-space data is measured, there is a necessary processing step called Nyquist ghost correction that is performed on it in order to turn it into the k-space data seen in Figure 8.9c. A Nyquist ghost is a standard artifact that occurs in GRE-EPI due to a phase discrepancy between the odd and even frequency encode direction (right-to-left and left-to-right) lines of k-space.

The raw k-space measurements from an unprocessed experimental fMRI scan are presented in Figure 8.11c and are reconstructed into an image by the same discrete inverse Fourier transform process in Figure 8.11 and as in Figure 8.7 and Figure 8.9. Note the prominent ghost of the brain at the top and bottom of the real and imaginary images in Figure 8.11a. Images with the Nyquist ghost as presented are not suitable for either visual interpretation or statistical analysis. We can compare Figure 8.11a with the Nyquist ghost to the improved reconstructed image in Figure 8.10a, which is after a correction. Nyquist ghost correction will be described later in this Section.

The magnitude and phase of the reconstructed raw experimental k-space data in Figure 8.11 are presented in Figure 8.12. Again, note the prominent Nyquist ghost of the brain at the top and bottom of the magnitude image in Figure 8.12a as compared to the image

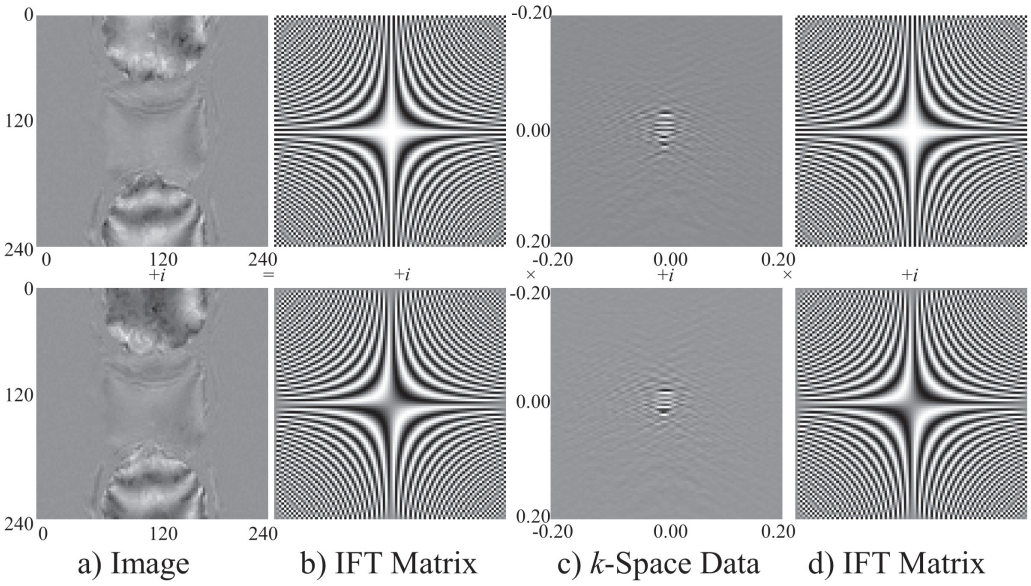

FIGURE 8.11
Reconstructed raw k-space data with Nyquist ghost.

after Nyquist ghost correction in Figure 8.10a. Images such as those in Figure 8.11a with the Nyquist ghost present are not suitable for either visual interpretation or statistical analysis.

Several methods have been developed to reduce such Nyquist ghosts (8, 9). Here, a method based upon the use of three navigator echoes, which allow the estimation and correction of the phase discrepancy (10) will be described. Before describing the three navigator echoes correction procedure, a little more explanation of the phase discrepancy and navigator echoes is in order. As previously noted, the Nyquist ghost occurs when there is a phase discrepancy between the odd and even lines of k-space. This phase discrepancy between the odd and even lines is illustrated in Figure 8.13a. Note that the array points are not aligned in the odd versus even lines in Figure 8.8a. The goal of the Nyquist ghost correction is to turn Figure 8.13a into Figure 8.8b.

In order to correct the phase discrepancy Δ, we first have to be able to estimate it. The Nyquist ghost phase discrepancy is echoes with the use of navigator. A navigator echo is a duplicate measurement of the entire $k_y = 0$ frequency encode line of k-space. In Figure 8.13b there are three navigator echoes presented, two from left to right and one from right to left. These navigator echoes could be measured at the beginning of the acquisition before the G_y phase encode gradient or in the middle of the acquisition when the center $k_y = 0$ line is being measured.

The process to experimentally estimate the phase discrepancy is to take each of the complex-valued navigator echo lines, labeled nav_1, nav_2, and nav_3, and one-dimensional discrete Fourier transform each of them to get NAV_1, NAV_2, and NAV_3. We also one-dimensional discrete Fourier transform each of the k-space lines for the entire array. Then we calculate

$$\hat{\omega}_0 = \text{angle}(NAV_3./NAV_1) \tag{8.15}$$

$$\hat{\phi} = NAV_2. * \exp(-i. * \hat{\omega}_0/2)./NAV_1 \tag{8.16}$$

$$\hat{\Delta} = \text{angle}(\text{median}(\text{real}(\hat{\phi})) + i\ \text{median}(\text{imag}(\hat{\phi}))) \tag{8.17}$$

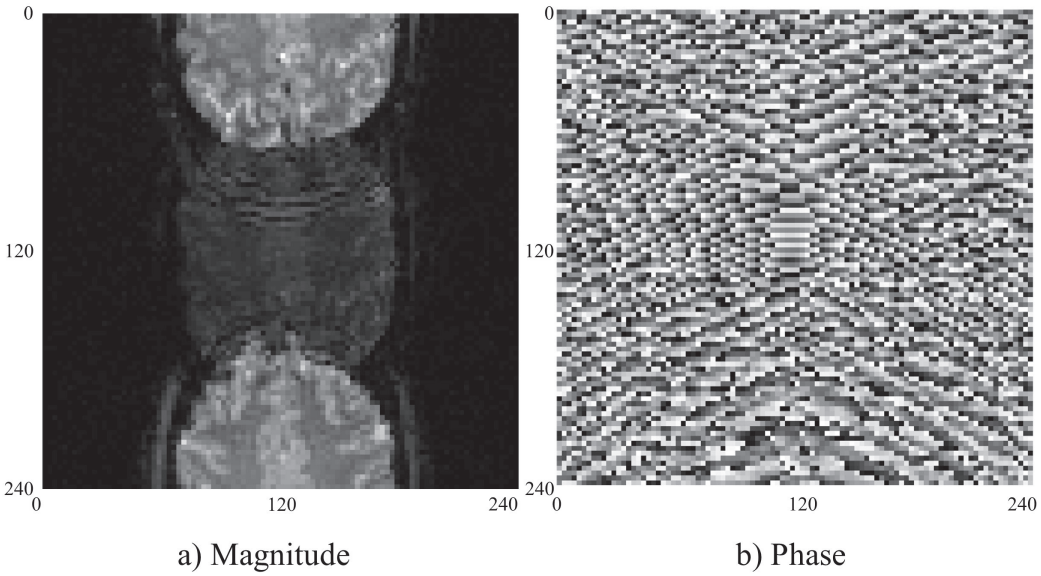

FIGURE 8.12
Magnitude and phase of reconstructed raw k-space data with Nyquist ghost.

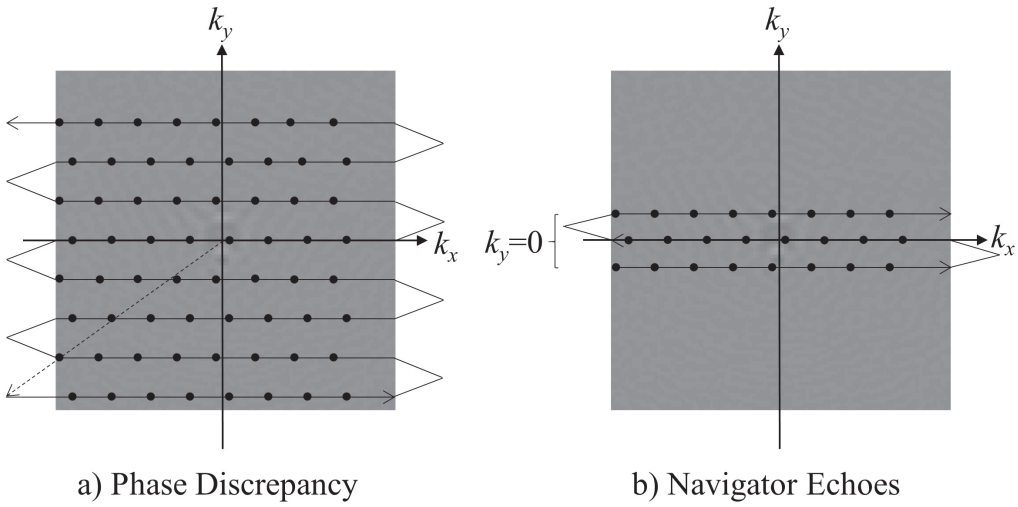

FIGURE 8.13
Odd and even line phase discrepancy and navigator echoes.

where angle(·) indicates calculating the angle of its complex-valued argument, .∗ indicates pointwise multiplication, ./ indicates pointwise division, median(·) returns the median if its vector argument, real(·) returns the real part of its argument, and imag(·) returns the imaginary part of its argument. Both $\hat{\Delta} = \text{angle}(\text{mean}((\hat{\phi})))$ and $\hat{\Delta} = \text{angle}(\text{median}((\hat{\phi})))$

have been utilized, but the median of the individual complex parts in Equation 8.17 works best experimentally.

Once the phase discrepancy is estimated to be $\hat{\Delta} = 0.4981$, the process to correct the k-space lines in Figure 8.13a is to one-dimensional discrete Fourier transform each row of k-space, and multiply the points in the odd lines by $\exp(-i\hat{\Delta})$ to shift them. Each of these corrected one-dimensional discrete Fourier transformed rows are now one-dimensional discrete inverse Fourier transformed with the result being the corrected rows of k-space as in Figure 8.9c. The corrected rows of k-space yield the real and imaginary images in Figure 8.9a and magnitude and phase in Figure 8.10 after image reconstruction.

As was demonstrated in this section, Nyquist ghost correction is a necessary processing operation in the display and analysis of fMRI experimental data. There are other processing operations performed on fMRI data that many find useful. These processing operations have been implemented to improve the statistical analysis, but the statistical ramifications of the processing are not well known. Any processing changes the statistical properties of the fMRI data. The AMMUST framework (11) is described in the next section and utilized to quantify the effect of select processing operations.

8.4 Image Processing

As was previously described, in MRI the data are Fourier encoded (4). The two-dimensional discrete inverse Fourier transform was utilized to reconstruct a complex-valued image in Section 8.3. In this section, the two-dimensional discrete inverse Fourier transform will be represented as a real-valued isomorphism involving the pre-multiplication of a vector of k-space data by a single inverse discrete Fourier transform matrix. Once this relationship is established, image processing can be represented as matrix multiplications and the resulting statistical properties can be quantified.

8.4.1 Reconstruction Isomorphism Representation

The discrete two-dimensional inverse Fourier transform in Equation 8.11 can be represented in terms of a single vector of spatial frequencies and a larger two-dimensional discrete inverse Fourier transform matrix (12). Let $f_R = \text{vec}(F_R')$ and $f_I = \text{vec}(F_I')$ be vectors of real and imaginary spatial frequency parts where $\text{vec}(\cdot)$ is defined to be the vectorization operator that stacks the columns of its matrix argument. The matrices F_R and F_I are the real and imaginary parts of the complex-valued spatial frequency matrix as described in Equation 8.11.

Then, we can perform a two-dimensional discrete inverse Fourier transformation as

$$\begin{array}{ccccc} \begin{pmatrix} y_R \\ y_I \end{pmatrix} & = & \begin{pmatrix} \Omega_R & -\Omega_I \\ \Omega_I & \Omega_R \end{pmatrix} & \begin{pmatrix} f_R \\ f_I \end{pmatrix} \\ y & = & \Omega & f \end{array} \tag{8.18}$$

where $y_R = \text{vec}(Y_R')$ contains the rows of the real part of the reconstructed image, $y_I = \text{vec}(Y_I')$ contains the rows of the imaginary part of the reconstructed image, and Ω is given by

$$\begin{array}{rcl} \Omega_R & = & \left[\left(\Omega_{yR} \otimes \Omega_{xR}\right) - \left(\Omega_{yI} \otimes \Omega_{xI}\right)\right] \\ \Omega_I & = & \left[\left(\Omega_{yR} \otimes \Omega_{xI}\right) + \left(\Omega_{yI} \otimes \Omega_{xR}\right)\right] \end{array} , \tag{8.19}$$

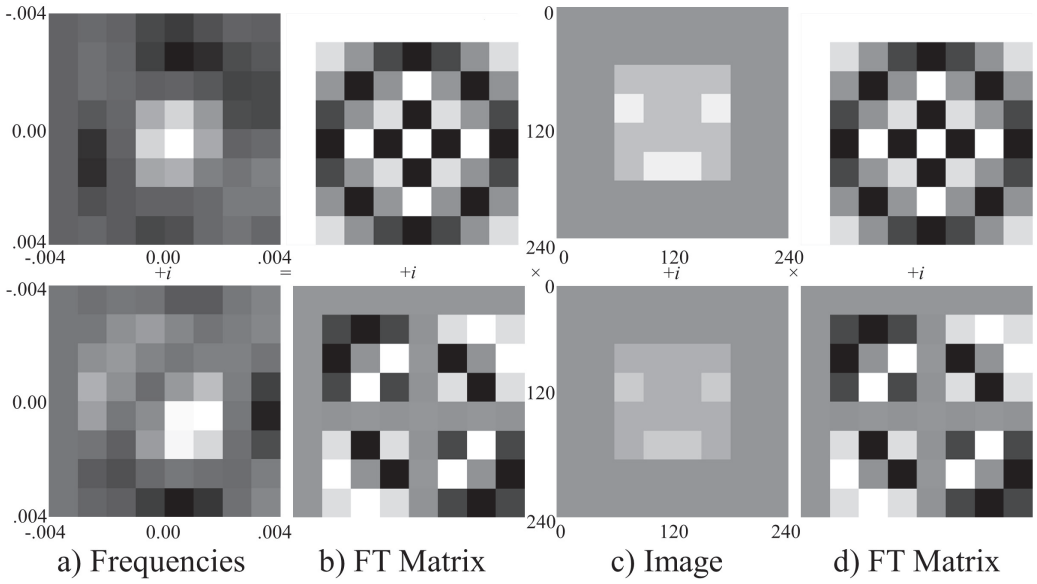

FIGURE 8.14
Image and spatial frequencies for illustrative isomorphism example.

where $\otimes$ is the Kronecker product that multiplies every element of its first matrix argument by its entire second matrix argument. In Equation 8.18, f and y are $2N_xN_y \times 1$ vectors and Ω is a $2N_xN_y \times 2N_xN_y$ matrix. The expression in Equation 8.19 was obtained by utilizing the result that the matrix multiplications $D = ABC$ can alternatively be expressed as $\text{vec}(D) = (C^T \otimes A)\text{vec}(B)$, so the two-dimensional discrete inverse Fourier transform in Equation 8.10 after attention to real and imaginary parts yields Equation 8.18 and Equation 8.19.

To illustrate the isomorphism representation of the two-dimensional discrete inverse Fourier transform, consider a small example involving the reconstruction of an 8×8 image as in Figure 8.14. In Figure 8.14c is the complex-valued 8×8 image, while Figure 8.14b and Figure 8.14d contain the two-dimensional discrete inverse Fourier transform matrices, in addition to Figure 8.14a containing the spatial frequencies.

In the isomorphism image reconstruction process, the spatial frequencies in Figure 8.14a are vectorized by stacking the rows of the real part of the frequencies on the rows of the imaginary part of the frequencies as displayed in Figure 8.15c and described in Equation 8.18. The two-dimensional discrete inverse Fourier transform matrices in Figure 8.14b and Figure 8.14d are utilized as in Equation 8.19 to form the single discrete inverse Fourier transformation matrix Ω as in Figure 8.15b. The vector of spatial frequencies f in Figure 8.15c is pre-multiplied by the larger two-dimensional discrete inverse Fourier transform matrix in Figure 8.15b to produce the vector of image voxel values y in Figure 8.15a. The vector of image voxel values in Figure 8.15a can be unstacked into the rows of the real part of the reconstructed image and the rows of the imaginary part of the reconstructed image as in Figure 8.14c.

The forward two-dimensional discrete Fourier transform can be performed in a similar fashion by multiplying the vector of stacked real and imaginary image rows by a single discrete forward Fourier matrix to obtain a vector of spatial frequencies that contains the

rows of the real on top of the rows of the imaginaries to form a complex-valued spatial frequency matrix that can be unstacked into the real and imaginary frequency matrices.

This inverse Fourier matrix and vectorized array representation is useful in examining the effects of preprocessing as we will see next.

8.4.2 Image Processing Implications

The isomorphism representation of the two-dimensional discrete inverse Fourier transform was utilized to represent image processing as matrix multiplications in the AMMUST (A Mathematical Model for Understanding the STatistical) effects framework (11). In the AMMUST framework, Equation 8.18 was extended as

$$y \quad = \quad O_I \quad \Omega \quad O_k \quad f \tag{8.20}$$

to include k-space and image processing operations as a matrix multiplication O_k and O_I or all operations performed on the original measurements as a single matrix $O = O_I \Omega O_k$.

It is known from multivariate statistics that if we have a vector f with mean vector $\mathrm{E}(f) = f_0$ and covariance matrix $\mathrm{cov}(f) = \Gamma$, and it is multiplied by a matrix O, then the mean of the resulting vector $y = Of$ has a new mean $\mu = Of_0$ and covariance matrix $\Sigma = O\Gamma O^T$. This means that we can analytically quantify how image processing written as a matrix multiplication changes the mean, variance, and correlation structure of our data under ideal conditions. This change of the statistical properties of our data including potential induced correlation is purely from image processing and reconstruction and of no biological origin.

There are many processing operations performed on the fMRI data. A few common processing operations are listed in Table 8.1. These processing operations are performed on

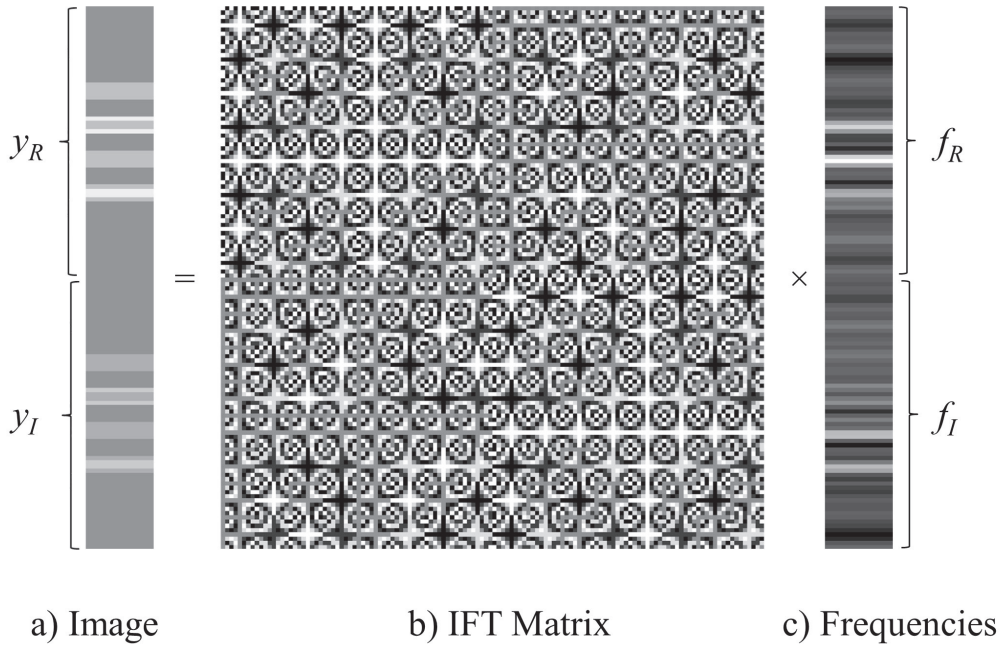

FIGURE 8.15
Image reconstruction via isomorphism representation.

TABLE 8.1
Some k-space, reconstruction, and image processing operations.

Image Space	**Reconstruction**	**k-space**
Image Smoothing	*Inverse Fourier*	Nyquist Ghost
Static $B0$ Correction	IP SENSE	Non-Cartesian Gridding
Global Normalization	IP GRAPPA	Motion Correction
Image Registration	TP SENSE	Ramp Sampling
	TP GRAPPA	Homodyne Interpolation
		Zero Filling
		Apodization

the fMRI data before any statistical analysis, often without the knowledge of the person carrying out the analysis. The processes that are italicized in Table 8.1 are examined in more detail first, then the other processes will be elaborated upon.

Zero filling, also known as zero fill interpolation, is the process of taking the spatial frequency array corresponding to an image and placing it at the center of a much larger array with zeros around it. Philosophically, it is equivalent to signifying that these higher spatial frequencies have been measured to be zero. The zero fill operator matrix Z can be formed by taking an identity matrix and removing the columns that correspond to k-space locations that are zero filled. Then the Kronecker product between a two-dimensional identity matrix I_2 and this column removed identity matrix is taken to form Z.

Apodization of k-space data is another common processing operation that has the goal to mitigate ripples in images after reconstruction, called Gibbs ringing. Gibbs ringing is an artifact from the measurement of a finite central region of frequencies that extend beyond those measured. This is often called a spatial frequency truncation effect. One common apodization process is to use a Tukey filter. The Tukey apodization filter in Equation 8.21

$$T(k) \quad = \quad \begin{cases} 1 & |k| < k_c \\ \cos^2\left(\frac{\pi(|k|-k_c)}{2w}\right) & k_c \leq |k| < k_c + w \\ 0 & k_c + w \leq |k| \end{cases} \tag{8.21}$$

is defined in k-space where $k = (k_x^2 + k_y^2)^{-1/2}$ is the distance from the center of k-space. In this, k_c is the radius below which there is no apodization, and w is the distance over which there are no apodization transitions to complete filtering. The rows of this matrix T are placed into a diagonal matrix to form the apodization operator A. The function in Equation 8.21 produces a radially symmetric disk gradually decreasing to zero that is centered at the center of k-space.

The two-dimensional discrete inverse Fourier transformation image reconstruction process was described as an operator Ω for matrix multiplication earlier in this section. It is a necessary processing step in the generation of images for interpretation and statistical analysis. It therefore can't be skipped, unlike the other processing operations (except for Nyquist ghost correction).

Image smoothing or blurring is a procedure that many image processors and analysts use. Its purpose is to mitigate discrepancies between subjects' brains, increase signal within voxels relative to noise, and help with Gaussianity (normal distribution) assumptions when using random field theory for activation map thresholding. The Gaussian image smoothing kernel G defined in image space is described as

$$G(r) \quad = \quad \frac{1}{2\pi\sigma^2}\exp\left(-\frac{r^2}{2\sigma^2}\right) \tag{8.22}$$

where $r = (x^2 + y^2)^{-1/2}$ is the distance from the center of the voxel of interest and

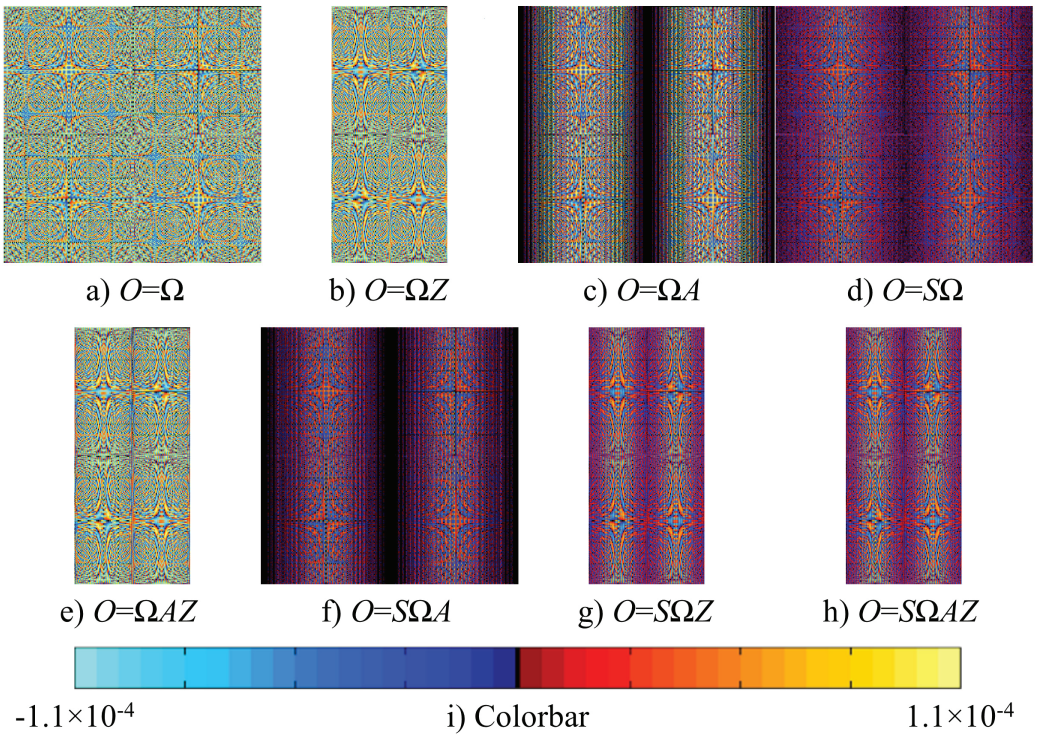

FIGURE 8.16
AMMUST processing operators, O.

$\sigma^2 = (\text{FWHM}/2)^2/(2\log 2)$ is the variance of a normal distribution, with FWHM denoting the full-width-at-half-max. The function in Equation 8.22 produces a radially symmetric Gaussian hill centered at the voxel of interest.

In order to gain some intuition into the processing and reconstruction operators, combinations of the four individual image processing operators Z, A, Ω, and S will be applied to an example for a typical size. Since we will want to reconstruct an image, the image reconstruction operator Ω will be included in all cases. The 96×96 k-space data in Figure 8.9c will be utilized as the mean image (f_0). When zero filling is applied, the central 64×64 portion of the k-space data in Figure 8.9c will be utilized and zero filled to 96×96. When apodization is applied, as in Equation 8.21, $k_c = 30$ and $w = 15$. All k-space data will be reconstructed to image space using the Ω operator as described in Equation 8.19 for 96×96 images. When smoothing is applied, a 2-voxel (5-mm) FWHM as described in Equation 8.22 will be used.

The processing and reconstruction operators are visually presented in Figure 8.16. The operator for only image reconstruction ($O = \Omega$) is given in Figure 8.16a; for zero filling from 64 to 96 and image reconstruction ($O = \Omega Z$) in Figure 8.16b; for apodization and image reconstruction ($O = \Omega A$) in Figure 8.16c; for image reconstruction and image smoothing ($O = S\Omega$) in Figure 8.16d; for zero filling, apodization, and image reconstruction ($O = \Omega AZ$) in Figure 8.16e; for apodization, image reconstruction, and image smoothing ($O = S\Omega A$) in Figure 8.16f; for zero filling, image reconstruction, and smoothing ($O = S\Omega Z$) in Figure 8.16g; and for zero filling, apodization, image reconstruction, and image smoothing ($O = S\Omega AZ$) in Figure 8.16h. All operator images are on the same intensity scale, $\pm 1.1 \times$

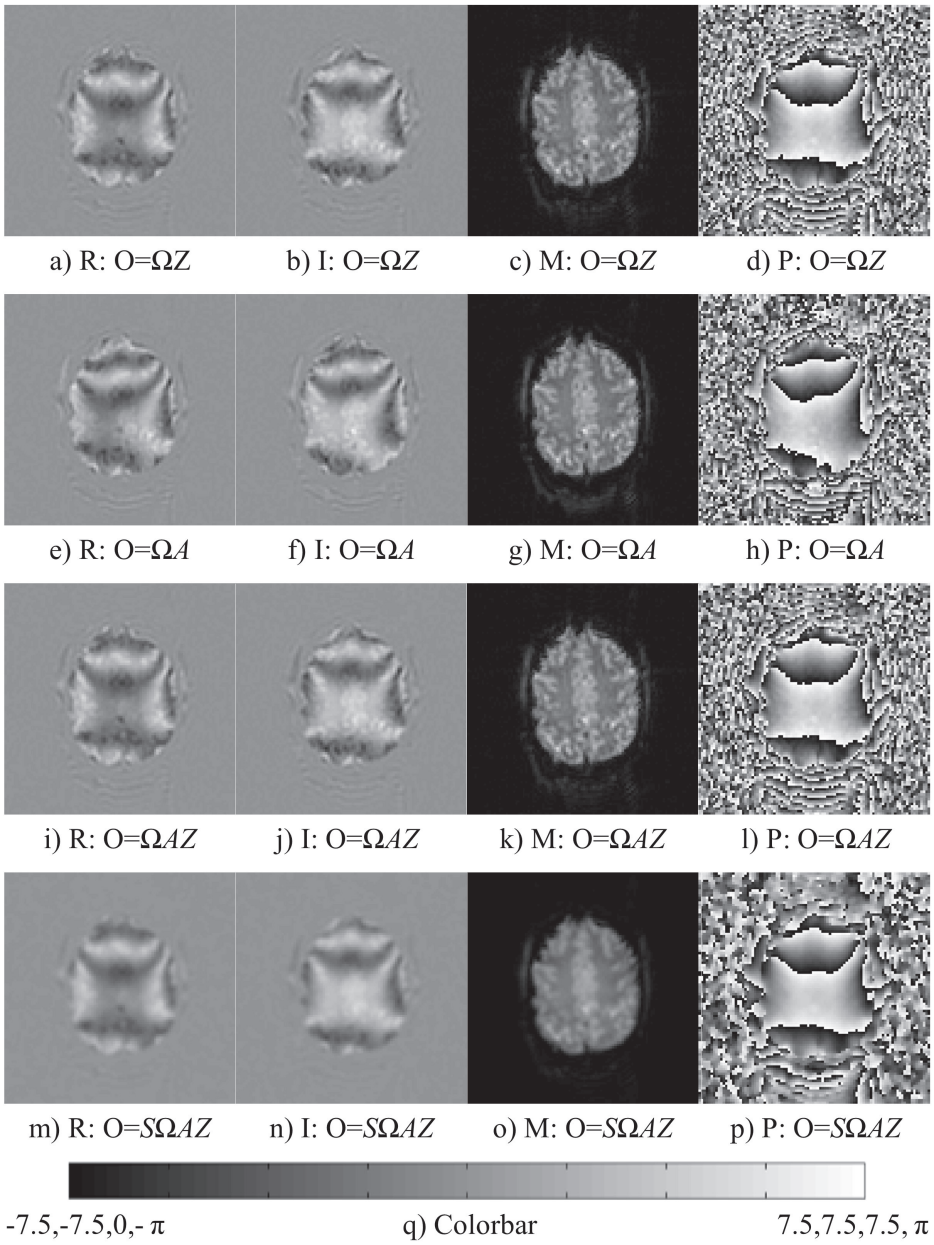

FIGURE 8.17
Modified mean images from processing.

10^{-4} with the same color bar for the operators given in Figure 8.16i. Note the differences between the operators as some appear in the green hues while others in the purple hues.

The mean real and imaginary images, along with the magnitude and phase derived from them, are shown Figure 8.17 for the various processing pipelines. The mean images for reconstruction only ($O = \Omega$) are presented in Figure 8.9 and Figure 8.10 and thus not repeated here. The mean images for $O = S\Omega$, $O = S\Omega A$, and $O = S\Omega Z$ are also not shown

as they are visually similar to the $O = S\Omega AZ$ mean images in Figures 8.17m–p, however, their magnitude of means are presented in Figure 8.18 as underlays.

The mean images after operator processing and reconstruction are visually presented in Figure 8.17. When applying zero filling from 64 to 96 and image reconstruction ($O = \Omega Z$) was performed, it yielded the mean real image in Figure 8.17a, the mean imaginary image in Figure 8.17b, the mean magnitude image in Figure 8.17c, and the mean phase image in Figure 8.17d. Note that the mean images after zero filling and reconstruction in Figures 8.17a–d appear slightly blurrier than those from solely reconstruction in Figure 8.9 and Figure 8.10. When applying apodization and image reconstruction ($O = \Omega A$) it yielded the mean real image in Figure 8.17e, the mean imaginary image in Figure 8.17f, the mean magnitude image in Figure 8.17g, and the mean phase image in Figure 8.17h. The mean images in Figures 8.17e–f appear similar but have slightly less detail than those in Figures 8.17a–d. When applying zero filling, apodization, and image reconstruction ($O = \Omega AZ$) it yielded the mean real image in Figure 8.17i, the mean imaginary image in Figure 8.17j, the mean magnitude image in Figure 8.17k, and the mean phase image in Figure 8.17l. The mean images in Figures 8.17i–l are virtually indistinguishable from those in Figures 8.17a–d. When all processing and reconstruction operations are applied, zero filling, apodization, image reconstruction, and image smoothing ($O = S\Omega AZ$), it yielded the mean real image in Figure 8.17m, the mean imaginary image in Figure 8.17n, the mean magnitude image in Figure 8.17o, and the mean phase image in Figure 8.17p. Note that the mean images in Figures 8.17m–p are noticeably blurrier that those from the other processing and reconstruction pipelines. All real and imaginary images are intensity limited in $[-7.5, 7.5]$, all magnitude images are intensity limited in $[0, 7.5]$, while all phase images are intensity limited in $[-\pi, \pi]$ as seen with the greyscale color bar in Figure 8.17q.

The correlations resulting from the various processing pipelines are displayed in Figure 8.18 assuming k-space measurements are uncorrelated. For the correlations, the entire $\Sigma = OO^T$ matrix was computed and then turned into a correlation matrix R. Since these are very large matrices, it is difficult to see the detail within them. To remedy the large matrices, the correlation between a given voxel and all others can be computed. The aforementioned processing and reconstruction operations yield the same correlation between any given voxel and all others. Therefore, the correlation between the center $(49, 49)$ voxel and all others will be displayed as a correlation image thresholded at $TH = 0.001$ and superimposed upon the corresponding magnitude image (intensity limited in $[0, 7.5]$) for visual reference. The resulting operator-induced correlation for only image reconstruction ($O = \Omega$) is given in Figure 8.18a; for zero filling from 64 to 96 and image reconstruction ($O = \Omega Z$) in Figure 8.18b; for apodization and image reconstruction ($O = \Omega A$) in Figure 8.18c; for image reconstruction and image smoothing ($O = S\Omega$) in Figure 8.18d; for zero filling, apodization, and image reconstruction ($O = \Omega AZ$) in Figure 8.18e; for apodization, image reconstruction, and image smoothing ($O = S\Omega A$) in Figure 8.18f; for zero filling, image reconstruction, and smoothing ($O = S\Omega Z$) in Figure 8.18g; and for zero filling, apodization, image reconstruction, and image smoothing ($O = S\Omega AZ$) in Figure 8.18h. All correlation images are on the same intensity scale, ± 1 with the same color bar for the correlations given in Figure 8.18i.

Note the differences in color and pattern between the various processing-induced correlations. It should be noted that $\Omega\Omega' = \frac{1}{NxNy} I_{2NxNy}$ and that only reconstruction does not induce a correlation between voxels. When zero filling is performed, there is an extended sinc ripple correlation structure in Figures 8.18b, e, g and h. When image smoothing is applied, there is a central circular region of strongly induced correlation between the voxels. If one also thinks about what a combination of two individual operators in Figures 8.18b–d would look like, you can rationalize their combination in Figures 8.18e–g. It is also interesting to match the operators in Figure 8.16 to these correlations in Figure 8.18

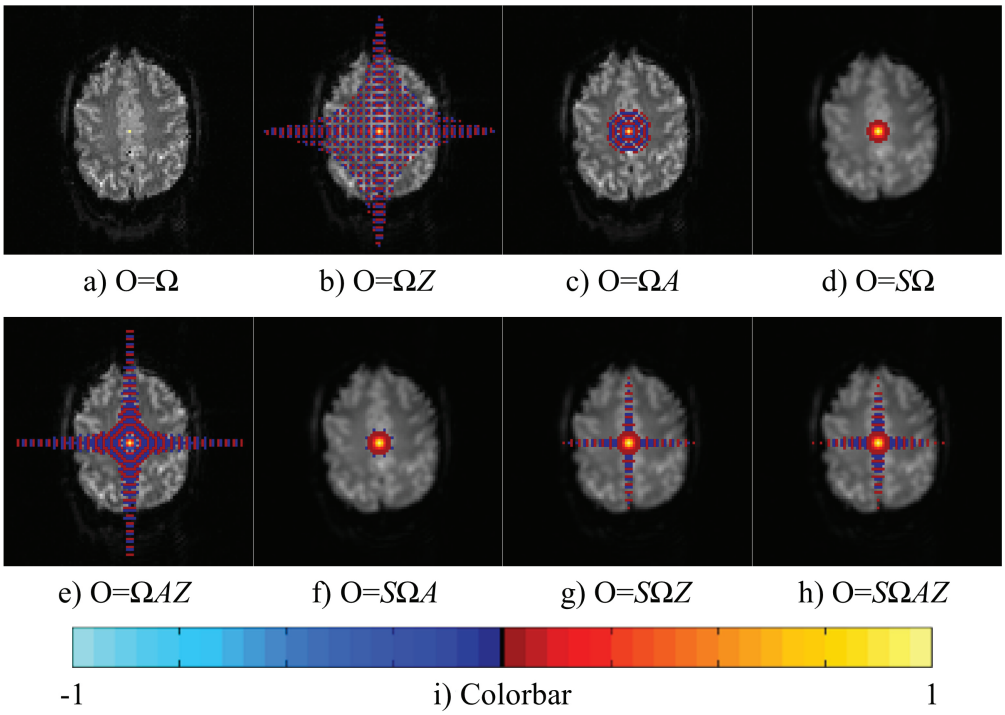

FIGURE 8.18
Modified correlations from image processing.

to see that when the operators appear generally similar, the induced correlations are also generally similar. The Nyquist ghost correction in Section 8.3 also does not induce a correlation in and of itself.

Additional k-space operators could be or have been developed for the remaining k-space processing operations in Table 8.1. Non-Cartesian gridding is a process where k-space is originally not on the Cartesian grid, such as the spiral trajectory (13) or polar sampling (14). Cartesian gridding is a linear process and a Cartesian gridding operator C could be developed to bring this irregularly measured data to the rectangular grid. Motion correction is a process to adjust for minor subject movement over time. In a rigid body transformation, an individual image is translated and rotated to match another image. Motion correction is a linear process and an operator M could be developed to examine its statistical properties. Ramp sampling is a process where the frequency encoding lines of k-space (horizontal in examples in this chapter) are not flat but linearly angled toward the next line to be measured. Ramp sampling interpolation estimates the angled k-space onto horizontal lines. It was empirically found that ramp sampling interpolation induces a local sinc type correlation between the voxels (15) but it is linear and a matrix operator could be developed. Homodyne interpolation is a process where the Hermitian property of k-space is utilized. Half of the k-space array is measured plus a little bit more, called over-scan lines, and the remaining portion is interpolated (16). It was shown that Homodyne interpolation does not change the image mean or correlation, but does increase voxel variances (11) and produces a purely real-valued image.

The AMMUST framework was utilized to examine the effects of in-plane (IP) k-space subsampling and image reconstruction with the SENSE (SENSitivity Encoding) (17) and

also the GRAPPA (GeneRalized Autocalibrating Partial Parallel Acquisition) (18) procedures. In the IP SENSE and GRAPPA reconstruction procedures, lines of k-space are skipped, which results in aliased reconstructed images. Additional full scans are measured, and with SENSE, the images are unaliased in image space with computed coil sensitivities while with GRAPPA, the missing lines of k-space are interpolated using a kernel. It was found that the use of SENSE and coil sensitivities induces a correlation between previously overlapping voxels (19) and that the use of GRAPPA with kernel interpolation also induces a correlation between previously overlapping voxels (20). These in-plane parallel image reconstruction procedures induce long-range correlations between the corresponding voxels in the previously overlapping image sections and additional image processing induces local correlation around these voxels. Care needs to be taken when interpreting these statistical results after either SENSE or GRAPPA in-plane acceleration reconstruction. Another avenue of image reconstruction that has been increasing in prominence is the selection of multiple slices for measurement resulting in k-space array images that are the sum of the arrays for the multiple slices. The measurement and separation of multiple overlapping slice images through-plane (TP) is called simultaneous multi-slice (SMS). The SENSE and GRAPPA unaliasing procedures are being applied TP and overlapping slice images separated. Since the same math and algorithms are being applied through-plane as in-plane, it is strongly believed that the same type of correlations will be induced through-plane into the separated slices and local correlations accentuated with image processing.

The effects of the remaining image space processing operations, have not been fully explored. Static $B0$ correction has been examined in simulations (21) but not for spatial statistical properties. Global normalization (22) and image registration (23) have yet to be examined and quantified. It is suspected that global normalization and image registration will induce a correlation between the voxels, but this has not been demonstrated. The quantification of image registration and global intensity normalization will provide an immense amount of knowledge to the field of fMRI as they are very common processing operations.

The AMMUST image processing framework was expanded (24) to stack k-space vectors from a time series of images, have a much larger matrix K of k-space processing to include different processing on each k-space vector, have a much larger matrix R that included reconstruction of each of the processed k-space vectors, and a much larger matrix I for processing on each of the reconstructed image vectors, then a matrix T that included first a permutation matrix so that the data is ordered by voxel and not by image along with a matrix that performs potentially different filtering of each of the time series as $O = TIRK$. It was found that time series processing such as frequency filtering induces a temporal correlation in voxel time series.

It was shown that different processing pipelines yield images with means and correlations that are modified in various ways including induced local correlation. The null hypothesis of no correlation between voxels is no longer valid when processing is involved. With the statistical properties of our image data changed in a known quantifiable manner, the processing operation matrices should be able to be incorporated into a statistical model for improved estimation and inference.

8.5 Additional Topics and Discussion

There are many topics that naturally arise from image reconstruction and processing. In this section, activation from complex-valued time series will be briefly described followed by a general discussion of the chapter.

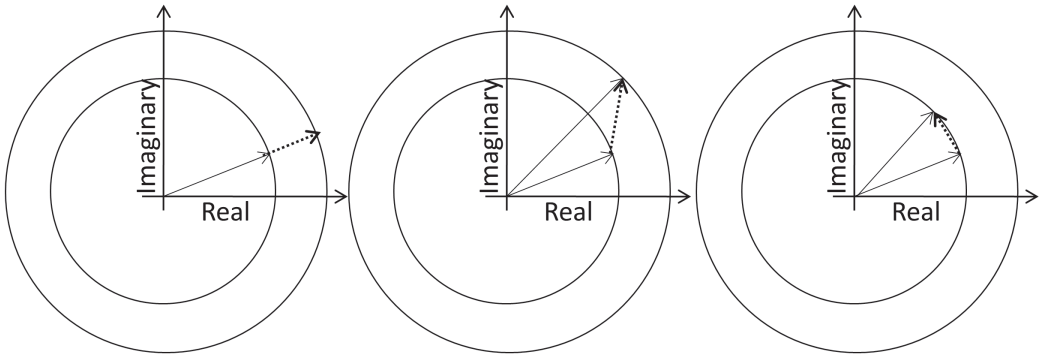

FIGURE 8.19
Complex-valued signal changes for activation.

8.5.1 Complex-Valued fMRI Activation

Since the image reconstruction methods yield complex-valued images, the time series within each voxel are also complex-valued. Models have been developed to detect three differential task-related changes in complex-valued fMRI time series.

Within complex-valued time series, there are three possible nonzero signal changes as shown in Figure 8.19. Figure 8.19a depicts a signal change only in the magnitude with a constant phase (CP), Figure 8.19b depicts a signal change in both the magnitude and phase (MP), and Figure 8.19c depicts a signal change only in the phase with a constant magnitude (CM). A CP activation model has been developed to detect statistically significant changes in the magnitude while specifying the phase is constant (25). An MP activation model has been developed where the full complex-valued (real-imaginary) data is utilized to detect statistically significant changes in both the magnitude and phase (26, 27).

For each voxel, the complex-valued measurement y_t at time t has been described as

$$\begin{aligned} y_t &= (\rho_t \cos\theta_t + \eta_{Rt}) + i(\rho_t \sin\theta_t + \eta_{It}) \\ \rho_t &= x_t'\beta = \beta_0 + \beta_1 x_{1t} + ... + \beta_{q_1} x_{q_1 t} \\ \theta_t &= u_t'\gamma = \gamma_0 + \gamma_1 u_{1t} + ... + \gamma_{q_2} x_{q_2 t} \end{aligned} \tag{8.23}$$

where $t = 1, \ldots, n$, $(\eta_{Rt}, \eta_{It})' \sim \mathcal{N}(0, \Sigma)$, x_t' is the t^{th} row of an $n \times (q_1 + 1)$ design matrix X for the magnitude, u_t' is the t^{th} row of an $n \times (q_2 + 1)$ design matrix U for the phase, and $\Sigma = \sigma^2 I_2$, while β and γ are magnitude and phase regression coefficient vectors respectively (26). Note that a separate design matrix U for the phase has been incorporated but X and U can be the same.

The usual fMRI activation model is a magnitude-only (MO) model where the phase images (and hence phase time series) are discarded (1). The MO model has been shown to be equivalent to a complex-valued activation model with unrestricted phase (28). A phase-only (PO) activation model, where the magnitude images (and hence the magnitude time series) are discarded, has been shown to detect statistically significant activation (12). When the phase images are discarded for the MO model, the MO model is not able to distinguish between CP signal changes in Figure 8.19a or MP signal changes in Figure 8.19b

because it does not have rotational phase information. Similarly, when the magnitude images are discarded, the PO model is not able to distinguish between CM signal changes in Figure 8.19c or MP signal changes in Figure 8.19b because it does not have lengthening magnitude information.

Voxel time series after image reconstruction are complex-valued. Discarding the phase half of the data, as is generally done with the usual magnitude-only model, may not be optimal in terms of statistical modeling and detection of biological processes. Future statistical analyses should utilize the full complex-valued fMRI data, and there are many opportunities for the discovery of biological phenomenon such as oxygenation changes in the vasculature (29, 30) or direct detection of neuronal currents (31, 32).

8.5.2 Discussion

In this chapter, the foundations and fundamentals of image reconstruction and image processing have been examined. In Section 8.2, the one- and two-dimensional discrete forward and inverse transformations were discussed. Knowledge of the Fourier transform is essential to understanding the original k-space measurements taken by the MRI scanner. In Section 8.3, the signal equation and the traversal of k-space along a trajectory was explained with the use of a pulse-sequence diagram so that the process of original k-space measurement could be understood. Also in Section 8.3, the raw unprocessed k-space measurements were described along with the very important Nyquist ghost correction. In Section 8.4, the two-dimensional discrete inverse Fourier transform process for image reconstruction was written in terms of an isomorphism so that it could be utilized to examine and quantify the statistical effects of reconstruction and image processing. It was demonstrated that some common fMRI processing steps induce local correlation and it was described that other reconstruction techniques induce long-range correlations. In Section 8.5, additional related topics of complex-valued activation for the reconstructed complex-valued images.

In summary, there are many processes performed on fMRI data before typical analysis, generally with no knowledge retained about what the processing was. It is hoped that knowledge of processing operations can be utilized in the statistical analysis of fMRI data.

Acknowledgments

This work was supported by National Institutes of Health research grant R21NS087450.

This material was based upon work partially supported by the National Science Foundation under Grant DMS-1127914 to the Statistical and Applied Mathematical Sciences Institute. Any opinions, findings, and conclusions or recommendations expressed in this material are those of the author(s) and do not necessarily reflect the views of the National Science Foundation.

Bibliography

[1] Bandettini P.A., Wong E.C., Hinks R.S., Tikofsky R.S, and Hyde J.S. Time course EPI of human brain function during task activation. *Magn Reson Med*, 25(2):390–397, June 1992.

[2] Kwong K.K., Belliveau J.W., Chesler D.A., Goldberg I.E., Weisskoff R.M. Poncelet B.P. Kennedy D.N., Hoppel B.E., Cohen M.S., and Turner R. Oxygenation-sensitive contrast in magnetic resonance image of rodent brain at high magnetic fields. *Proc Natl Acad Sci USA*, 89(12):5675–5679, June 1992.

[3] Ogawa S., Tank D.W., Menon R.S., Ellermann J.M. ad Kim S.G., Merkle H., and Ugurbil K. Intrinsic signal changes accompanying sensory stimulation: Functional brain mapping with magnetic resonance imaging. *Proc Natl Acad Sci USA*, 89(13):5951–5955, July 1992.

[4] Kumar A., Welti D., and Ernst R.R. NMR Fourier zeugmatography. *J Magn Reson*, 18(1):69–83, April 1975.

[5] Shannon C.E. Communication in the presence of noise. In *Proc Institute of Radio Engineers*, volume 37, pages 10–21. John Wiley and Sons, January 1949.

[6] Nyquist H. Certain topics in telegraph transmission theory. *Trans AIEE*, 47:617–644, April 1928. Reprint as classic paper in *Proc. IEEE*, 90(2), Feb 2002.

[7] Karaman M.M., Bruce I.P., and Rowe D.B. Incorporating relaxivities to more accurately reconstruct MR images. *Magn Reson Imaging*, 33(4):374–384, 2014.

[8] Jesmanowicz A., Wong E.C., and Hyde J.S. Phase correction for EPI using internal reference lines. In *Proc Soc Magn Reson Med*, volume 12, page 1239, New York, New York, 1993. John Wiley and Sons.

[9] Jesmanowicz A., Wong E.C., and Hyde J.S. Self-correcting EPI reconstruction algorithm. In *Proc Soc Magn Reson Med*, volume 14, page 619, Nice, France, 1995. John Wiley and Sons.

[10] Nencka A.S., Hahn A.D., and Rowe D.B. The use of three navigator echoes in Cartesian EPI reconstruction reduces Nyquist ghosting. In *Proc Intl Soc Magn Reson Med*, volume 16, page 3032, Toronto, Canada, 2008. John Wiley and Sons.

[11] Nencka A.S., Hahn A.D., and Rowe D.B. A mathematical model for understanding the statistical effects of k-space (AMMUST-k) preprocessing on observed voxel measurements in fcMRI and fMRI. *J Neurosci Methods*, 181(2):268–282, 2009.

[12] Rowe D.B., Nencka A.S., and Hoffmann R.G. Signal and noise of Fourier reconstructed fMRI data. *J Neurosci Methods*, 159(2):361–369, 2007.

[13] Ahn C.B., Kim J.H., and Cho Z.H. High speed spiral scan echo planar NMR imaging-I. *IEEE Trans Med Imaging*, 5(1):2–7, 1986.

[14] Lauzon M.L. and Rutt B.K. Polar sampling in k-space: Reconstruction effects. *Magn Reson Med*, 40(5):769–782, November 1998.

[15] Deshpande G., LaConte S., Peltier S., and X. Hu. Integrated local correlation: A new measure of local coherence in fMRI data. *Hum Brain Mapp*, 30(1):13–23, 2009.

[16] Jesmanowicz A., Bandettini P.A., and Hyde J.S. Single-shot half k-space high-resolution gradient-recalled EPI for fMRI at 3 Tesla. *Magn Reson Med*, 40(5):754–762, November 1998.

[17] Pruessmann K.P., Weiger M., Scheidegger M.B., and Boesiger P. SENSE: Sensitivity encoding for fast MRI. *Magn Reson Med*, 42(5):952–962, November 1999.

[18] Griswold M.A., Jakob P.M. Heidemann R.M., Nittka M., Jellus V., Wang J., Kiefer B., and Haase A. Generalized autocalibrating partially parallel acquisitions (GRAPPA). *Magn Reson Med*, 47(6):1202–1210, June 2002.

[19] Bruce I.P., Karaman M.M., and Rowe D.B. A statistical examination of SENSE image reconstruction via an isomorphism representation. *Magn Reson Imaging*, 29(9):1267–1287, 2011.

[20] Bruce I.P. and Rowe D.B. Quantifying the statistical impact of GRAPPA in fcMRI data with a real-valued isomorphism. *IEEE Trans Med Imaging*, 33(2):495–503, 2014.

[21] Hahn A.D., Nencka A.S., and Rowe D.B. Improving robustness and reliability of phase-sensitive fMRI analysis using Temporal Off-Resonance Alignment of Single-Echo Timeseries (TOAST). *Neuroimage*, 44(3):742–752, 2009.

[22] Friston K.J., Ashburner J., Frith C.D., Poline J.B., Heather J.D., and Frackowiak R.S.J. Spatial registration and normalization of image. *Hum Brain Mapp*, 3(3):165–189, 1995.

[23] Jenkinson M., Bannister P., Brady M., and Smith S. Improved optimization for the robust and accurate linear registration and motion correction of brain images. *Neuroimage*, 17(2):825–841, 2002.

[24] Karaman M.M., Nencka A.S., Bruce I.P., and Rowe D.B. Quantification of the statistical effects of spatiotemporal processing of non-task fMRI data. *Brain Connect*, 4(9):649–661, 2014.

[25] Rowe D.B. and Logan B.R. A complex way to compute fMRI activation. *Neuroimage*, 32(3):1078–1092, 2004.

[26] Rowe D.B. Modeling both the magnitude and phase of complex-valued fMRI data. *Neuroimage*, 25(4):1310–1324, 2005.

[27] Rowe D.B. Magnitude and phase signal detection in complex-valued fMRI data. *Magn Reson Med*, 62(5):1356–1357, 2009.

[28] Rowe D.B. and Logan B.R. Complex fMRI analysis with unrestricted phase is equivalent to a magnitude-only model. *Neuroimage*, 24(2):603–606, 2005.

[29] Menon R.S. Postacquisition suppression of large-vessel BOLD signals in high-resolution fMRI. *Magn Reson Med*, 47(1):1–9, 2002.

[30] Nencka A.S. and Rowe D.B. Reducing the unwanted draining vein BOLD contribution in fMRI with statistical post-processing methods. *Neuroimage*, 37(1):177–188, 2007.

[31] Bodurka J., Jesmanowicz A., Hyde J.S., Xu H., Estowski L., and Li S.-J. Current-induced magnetic resonance phase imaging. *J Magn Reson*, 137(1):265–271, 1999.

[32] Chow L.S., Cook G.G., Whitby E., and Paley M.N. Investigating direct detection of axon firing in the adult human optic nerve using MRI. *Neuroimage*, 30(3):835–846, 2006.